Role of inner solvation sheath within salt–solvent complexes in tailoring electrode/electrolyte interphases for lithium metal batteries

Xiaodi Ren[a,1,2], Peiyuan Gao[b,1], Lianfeng Zou[c], Shuhong Jiao[a,2], Xia Cao[a], Xianhui Zhang[a], Hao Jia[a], Mark H. Engelhard[c], Bethany E. Matthews[a], Haiping Wu[a], Hongkyung Lee[a,3], Chaojiang Niu[a], Chongmin Wang[c], Bruce W. Arey[a], Jie Xiao[a], Jun Liu[a], Ji-Guang Zhang[a,4], and Wu Xu[a,4]

[a]Energy and Environment Directorate, Pacific Northwest National Laboratory, Richland, WA 99354; [b]Physical and Computational Sciences Directorate, Pacific Northwest National Laboratory, Richland, WA 99354; and [c]Environmental Molecular Sciences Laboratory, Pacific Northwest National Laboratory, Richland, WA 99354

Functional electrolyte is the key to stabilize the highly reductive lithium (Li) metal anode and the high-voltage cathode for long-life, high-energy-density rechargeable Li metal batteries (LMBs). However, fundamental mechanisms on the interactions between reactive electrodes and electrolytes are still not well understood. Recently localized high-concentration electrolytes (LHCEs) are emerging as a promising electrolyte design strategy for LMBs. Here, we use LHCEs as an ideal platform to investigate the fundamental correlation between the reactive characteristics of the inner solvation sheath on electrode surfaces due to their unique solvation structures. The effects of a series of LHCEs with model electrolyte solvents (carbonate, sulfone, phosphate, and ether) on the stability of high-voltage LMBs are systematically studied. The stabilities of electrodes in different LHCEs indicate the intrinsic synergistic effects between the salt and the solvent when they coexist on electrode surfaces. Experimental and theoretical analyses reveal an intriguing general rule that the strong interactions between the salt and the solvent in the inner solvation sheath promote their intermolecular proton/charge transfer reactions, which dictates the properties of the electrode/electrolyte interphases and thus the battery performances.

solvation sheath | salt-solvent complex | interphase | LHCE | lithium metal battery

High-voltage (>4.0 V) lithium (Li) metal batteries (LMBs) are regarded as one of the most promising energy storage systems because of their much higher energy density as compared with conventional Li-ion batteries (LIBs) (1–3). On the anode side, Li metal is an ideal anode material with an ultrahigh specific capacity of 3,860 mAh g^{-1} as well as an extremely low electrochemical potential of −3.040 V (vs. standard hydrogen electrode). On the cathode side, state-of-the-art high-voltage Ni-rich cathodes, e.g., LiNi$_{0.8}$Mn$_{0.1}$Co$_{0.1}$O$_2$ (NMC811), can deliver a capacity over 200 mAh g^{-1}, much higher than those of LiFePO$_4$, LiCoO$_2$, or stoichiometric NMC111 materials (4). Therefore, LMBs with a structure of Li||NMC811 are expected to have specific energy densities over 500 Wh kg^{-1} on the cell level, nearly double those of LIBs currently used in electric vehicles (5). However, the applications of LMBs are still hindered by several obstacles. The highly reductive nature of Li metal anode (LMA) makes it prone to react with all polar solvents and salt anions used in batteries nowadays, although with varied degrees. This issue not only results in low Li Coulombic efficiencies (CEs) due to continuous side reactions during Li metal plating/stripping processes, but also is closely related to the uncontrolled Li dendrite growth, which imposes serious safety risks for battery applications (3). In addition, highly reactive transition-metal ions (e.g., Ni^{4+}) on cathode surfaces (especially Ni-rich cathodes) formed under delithiated state at high charge voltages can also induce severe side reactions with electrolytes (6). In fact, such

reactions were found to be one of the main factors for the degradation of NMC811 cathode under high voltages (7, 8).

The stability of LMA is largely dictated by the solid electrolyte interphase (SEI) generated on the Li metal surface in non-aqueous electrolytes (6). The SEI forms via a self-limiting reaction between the LMA and the electrolyte and acts as a kinetic barrier between them. Similarly, the cathode electrolyte interphase (CEI) plays an important role in suppressing side reactions between the catalytically active cathode and the electrolyte. As the compositions and the properties of the SEI and the CEI are directly related to the chemical nature of the electrolyte employed, the development of functional electrolytes for LMBs is critical to solve the stability challenges of reactive electrodes. In recent years, various electrolyte solvents, salts, and additives

Significance

Rechargeable lithium metal batteries are promising next-generation high-energy-density energy storage systems. However, their applications have been greatly impeded by the instabilities of electrolytes toward both highly reductive lithium metal anode and high-voltage cathodes. Here, we use localized high-concentration electrolytes to investigate the fundamental correlation between the battery performance and the electrolyte solvation chemistry and its profound electrode/electrolyte interphase properties. Experimental and theoretical analyses reveal an intriguing general rule that the strong interactions between the salt and the solvent in the inner solvation sheath within the salt–solvent complexes promote their intermolecular proton/charge-transfer reactions, dictate the properties of the electrode/electrolyte interphases, and then influence the battery performances. These findings can shed light for rational electrolyte design for various battery systems.

have been proven beneficial for improving the performance of LMBs (9–15). In particular, as one of the most important concepts in recent electrolyte development, high-concentration electrolytes (HCEs) (or superconcentrated electrolytes) have demonstrated their compatibility with both the LMA and the high-voltage cathodes (16–21). Different from conventional low concentration electrolytes (LCEs) with large proportions of free solvents and salt anions (Fig. 1A), HCEs with high salt/solvent ratios have not enough free-solvent molecules to fully solvate Li^+ ions in the electrolytes. As a result, salt anions are drawn into the inner solvation sheath by electrostatic attractions (Fig. 1B). It is commonly accepted that the lowest unoccupied molecular-orbital (LUMO) energies of the anions shift to a value lower than those of the solvent in an HCE. Therefore, the anion in the electrolyte will be reduced first to form an inorganic compounds (such as LiF, Li_2O)-rich SEI layer which can effectively improve the stability of the LMA (19). At the same time, the downward shift of the highest occupied molecular-orbital (HOMO) energies of coordinated solvent molecules and the scarcity of free-solvent molecules basically prohibit electrolyte oxidations and thus cathode corrosions. In both scenarios, the role of solvent molecules in HCEs in the interfacial reactions is often treated as solitary or even trivial. Nevertheless, previous models have fallen short to explain the critical salt–solvent synergy in HCEs discovered recently (22). Therefore, further studies of the interaction mechanism in the "crowded" solvation sheath are of great importance to understand the stability of electrodes in different electrolytes.

The latest development of localized high-concentration electrolytes (LHCEs) has shown great promise for further advancing the HCEs and promoting the practical application of LMBs (23–26). In the LHCE, the addition of nonsolvating diluent molecules in the HCE creates a unique solvation structure, where the overall solvation features of the HCE are retained in the inner solvation sheath and the diluent forms an outer nonsolvating sphere, as shown in Fig. 1C. With the proper selection, the diluent can have a good miscibility with the inner solvation sheath due to the dipole–dipole interactions. It should be noted that the nonsolvating diluent outer sphere not only improves the physical properties of the LHCE (e.g., viscosity and wettability) for battery applications compared to the HCE, but also shields cations and anions in the inner solvation sheath from electrostatic attractions of ions in nearby solvation complexes. As a result, cation–anion and ion–solvent interactions in the inner solvation sheath of LHCE are further enhanced. This phenomenon has been evidenced by different experimental observations lately: the further deviation from the "ideal" KCl line in Walden plots (indicating fully dissociated ions) and the distinctive chemical shifts of coordinating oxygen atoms from ^{17}O-NMR spectra, compared to those in parallel HCEs (24, 27, 28). Therefore, the LHCE system can serve as a unique platform for investigating the properties of the inner solvation sheath and its role in the interfacial reaction processes between electrodes and electrolytes.
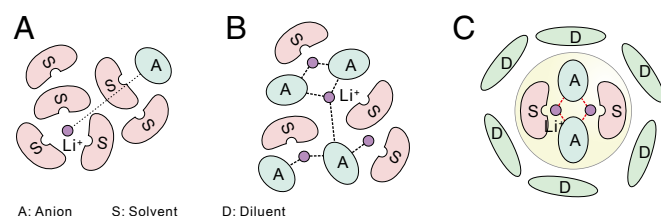
Although different combinations of solvating solvents and diluents have been used to prepare LHCEs, previous studies mainly focused on their capabilities of improving physical properties of conventional HCEs, e.g., lower viscosity, higher ion conductivity, better wettability, wider operation temperature window, lower polysulfide dissolution in Li-sulfur batteries, etc. (23–25, 29–31) The critical role of the inner solvation sheath within salt–solvent complexes on the electrode/electrolyte interfacial stabilities is not well understood. In this work, we systematically investigated LHCEs based on four different types of model solvents for battery applications, including dimethyl carbonate (DMC), tetramethylene sulfone (TMS), triethyl phosphate (TEP), and 1, 2-dimethoxyethane (DME), in order to explain the underlying mechanisms for their different behaviors on both the LMA and the cathode. Experimental results show that the solvent molecules, despite their low proportion in the LHCE, in the inner solvation sheath have important implications on the stability of electrode interphases, especially on the high-voltage cathode. Further theoretical calculations indicate that the proton/charge-transfer reactions between the salt and the solvent in the inner solvation sheath play an important role in the interfacial chemistries and have a significant effect on the cycling stability of the battery. With this effect, the LHCEs based on the ether solvent, which is often considered as an unstable solvent to be used in high voltage (over 4 V) batteries, demonstrate the best performances on both the LMA and the NMC811 cathode under a high voltage of 4.4 V. This study reveals another dimension in the electrolyte solvation chemistry and provides a strategy on how to manipulate the inner solvation structure of the electrolytes and further improve the stability of electrolytes in a wide electrochemical window.

Results and Discussion

In order to investigate the effects of different types of coordinating solvents on the stabilities of the LMA and the metal oxide cathode NMC811, four solvating solvents, DMC, TMS, TEP, and DME, covering the four typical solvent systems—carbonate, sulfone, phosphate, and ether, relevant for high-voltage LMB applications—are selected (32). The Li salt is lithium bis(-fluorosulfonyl)imide (LiFSI), a popular salt for LMBs in recent years, which offers excellent Li protection capability in a variety of HCEs. TTE (1, 1, 2, 2-tetrafluoroethyl-2,2,3,3-tetrafluoropropyl ether) is selected as the diluent (that has negligible solvability for LiFSI salt), which exhibits a reasonable boiling point (93 °C) and low cost, and has demonstrated good performances in the LHCEs (24, 26). When the molar ratio of LiFSI to TTE is fixed as 1:3, the molar content of the coordinating solvent in the corresponding LHCE depends on the solvent properties like the solvating capability with LiFSI and the mixability with TTE, etc. For a fair comparison, the amount of the solvating solvent is adjusted to near the salt saturation but with an excessive ratio of ~5% in order to reduce the number of uncoordinated solvent molecules and also to avoid the precipitation of clusters during testing. It should be noted that due to the varied salt–solvent coordination geometries in different LHCEs, the exact molar ratios between the LiFSI salt and the solvating solvent molecules are different. However, nearly all solvent molecules are coordinated with the LiFSI salt for better electrochemical performances. The electrolyte formulations of these four LHCEs are LiFSI-2.2DMC-3TTE, LiFSI-1DME-3TTE, LiFSI-1.4TEP-3TTE, and LiFSI-3TMS-3TTE, and their physical properties are shown in *SI Appendix*, Table S1. The snapshots of the chemical structures of the four LHCEs are shown in Fig. 2, which illustrates that these LHCEs have different clusters of Li salt with coordinating solvent molecules and these clusters are separated by the noncoordinating diluent molecules. The radial distribution functions (RDFs) in Fig. 2 also indicate the high salt/solvent ratio renders that nearly all solvent molecules are coordinated with Li^+ ions and salt anions, while the diluent molecules are mostly excluded from the inner ion solvation
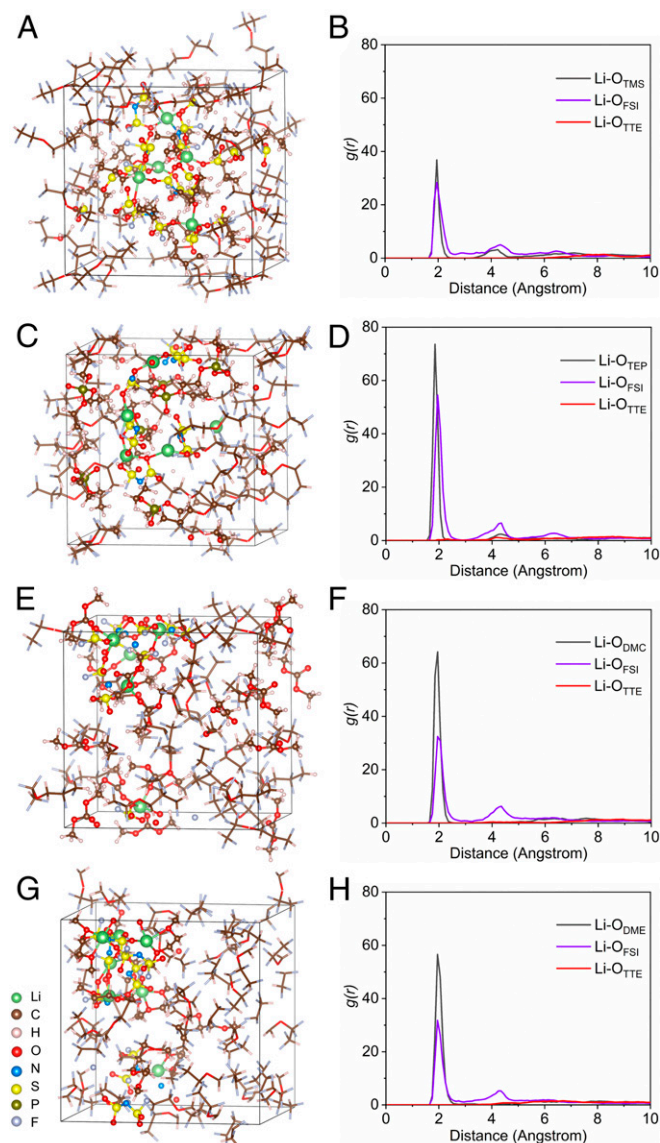

Fig. 1. Schematic illustrations of solvation structures in different types of electrolytes: (A) LCE, (B) HCE, (C) LHCE. The electrostatic interactions between Li^+ and anions are indicated by dotted arrows.

Fig. 2. AIMD simulation snapshots of different LHCE systems and the corresponding RDFs (*A* and *B*) TMS-LHCE, (*C* and *D*) TEP-LHCE, (*E* and *F*) DMC-LHCE, and (*G* and *H*) DME-LHCE. (For clarity purposes, the salt–solvent clusters are displayed in ball-stick model and the diluent molecules in line model.)

sheath because of their poor ion-solvating capability. As a result, the favorable reactivity characteristics of HCEs can be retained in the LHCEs.

To evaluate the stability of LMA in these four LHCEs, the average CEs of Li plating/stripping in Li||Cu cells were measured using a 10-cycle average protocol combined with a preconditioning cycle, as described in our previous report (33). All four LHCEs have high Li CEs over 99%, confirming that this dilution strategy works well with HCEs in maintaining their desired Li metal stability as well as limiting Li loss from electrolyte side reactions and "dead" Li formations. On the other hand, the average Li CEs still show some variations depending on the coordinating solvent selected (Fig. 3*A*), which follow the order as: 99.1% (TEP-LHCE) < 99.2% (TMS-LHCE) < 99.3% (DMC-LHCE) < 99.5% (DME-LHCE). In long-term cycling of symmetric Li||Li cells in different LHCEs, variations of voltage profiles can also be observed (*SI Appendix*, Table S1). This suggests that the solvating solvents do

influence the Li metal/electrolyte interfacial chemistry, and the detailed explanations will be discussed in later sections (e.g., *Li/ Electrolyte Interphase* and *Simulations on Electrolyte Systems*).

The electrochemical oxidation stabilities of the studied LHCEs were further evaluated using Super P (SP)-based electrodes [made of SP carbon and polyvinylidene fluoride (PVDF) binder coated on aluminum (Al) foil] as the working electrode and Li metal as the counter electrode in a coin-cell setup and the results are shown in Fig. 3*B*. At the voltage of 4.4 V, the response current densities for the above LHCEs are 3.53, 3.35, 3.00, and 2.57 $\mu A\ cm^{-2}$ for DMC-LHCE, DME-LHCE, TMS-LHCE, and TEP-LHCE, respectively. For the DME-LHCE, the slope of the oxidation current curve begins to increase above 4 V before the exponential increase over 4.5 V. It is possible that the initial decomposition of the DME-LHCE induces the passivation of the SP electrode, which will be further discussed later. Overall, on the relatively active SP electrode, despite small differences of oxidation currents, all four LHCEs do not show excessive decompositions at 4.4 V. Although ethers are typically unstable above 4 V, the high salt/ether ratio is effective in enhancing their anodic stability, agreeing with previous studies (20, 22).

To evaluate the stability of electrolytes in a more practical conditions required for high-energy LMBs, Li||NMC811 cells were investigated with different LHCEs under a high charge cutoff voltage of 4.4 V. As shown in Fig. 3*C*, the overall voltage-capacity profiles of the cells in the first formation cycle (at C/10 rate) are very similar when different LHCEs are used, except in the case of TEP-LHCE electrolyte. The fine difference is better illustrated by the dQ/dV curve shown in Fig. 3*D*, where two anodic peaks at higher potentials (∼3.70 and 3.79 V) for TEP-LHCE are better resolved than other LHCEs' peaks. These two peaks represent the oxidation of mixed Ni^{2+}/Ni^{3+} into Ni^{4+} accompanying phase-transition processes during delithiation (8). The cycling performances of Li||NMC811 cells in different LHCEs are compared in Fig. 3*E*. Based on the conventional understanding, the electrolytes with higher anodic stabilities (>4 V), such as DMC, TMS, and TEP, will have better stability at high voltage conditions than those with DME when these solvents were used separately. However, LHCEs using DMC, TMS, and TEP actually lead to inferior long-term cycling stabilities compared to the LHCE based on DME as shown in Fig. 3*E*. Similar to what we demonstrated previously (22), a high molar ratio of LiFSI/ether can greatly inhibit the decomposition of the ether molecules with a decreased HOMO energy level and an effectively protective CEI layer. With a LiFSI/DME molar ratio of 1:1 in the DME-LHCE, the average CE of Li||NMC811 cell over 300 cycles can reach 99.8%, which is very close to that in the TEP-LHCE (99.9%) and higher than those in the DMC-LHCE (99.7%) and TMS-LHCE (99.3% for 300 cycles, 99.8% for first 200 cycles) (*SI Appendix*, Fig. S2). The Li||NMC811 cell with DME-LHCE retained ∼90% capacity and exhibited stable voltage profiles (*SI Appendix*, Fig. S3) over 300 cycles, while those with DMC-LHCE, TMS-LHCE, and TEP-LHCE retained only 56, 13, and 85% capacity, respectively, as shown in Fig. 3*E* and *SI Appendix*, Fig. S3.

Electrochemical impedance spectroscopy was used to monitor the impedance changes in the Li||NMC811 cells during cycling. The Nyquist plots obtained after 20th, 50th, and 100th discharge cycles are compared in *SI Appendix*, Fig. S4. The higher-frequency semicircle is usually related to the Li^+ diffusion process, especially the Li^+ diffusion across the Li anode passivation layer in this case, while the lower-frequency semicircle is related to the interfacial charge-transfer process, particularly the cathode charge transfer in this case. From the fitting results (*SI Appendix*, Table S2 and Fig. S4 *E* and *F*), it is clear that the most apparent change of Li^+ diffusion resistance is in the DMC-LHCE, followed by the TEP-LHCE. The scanning electron microscopy (SEM) images of the Li anodes after 100 cycles show
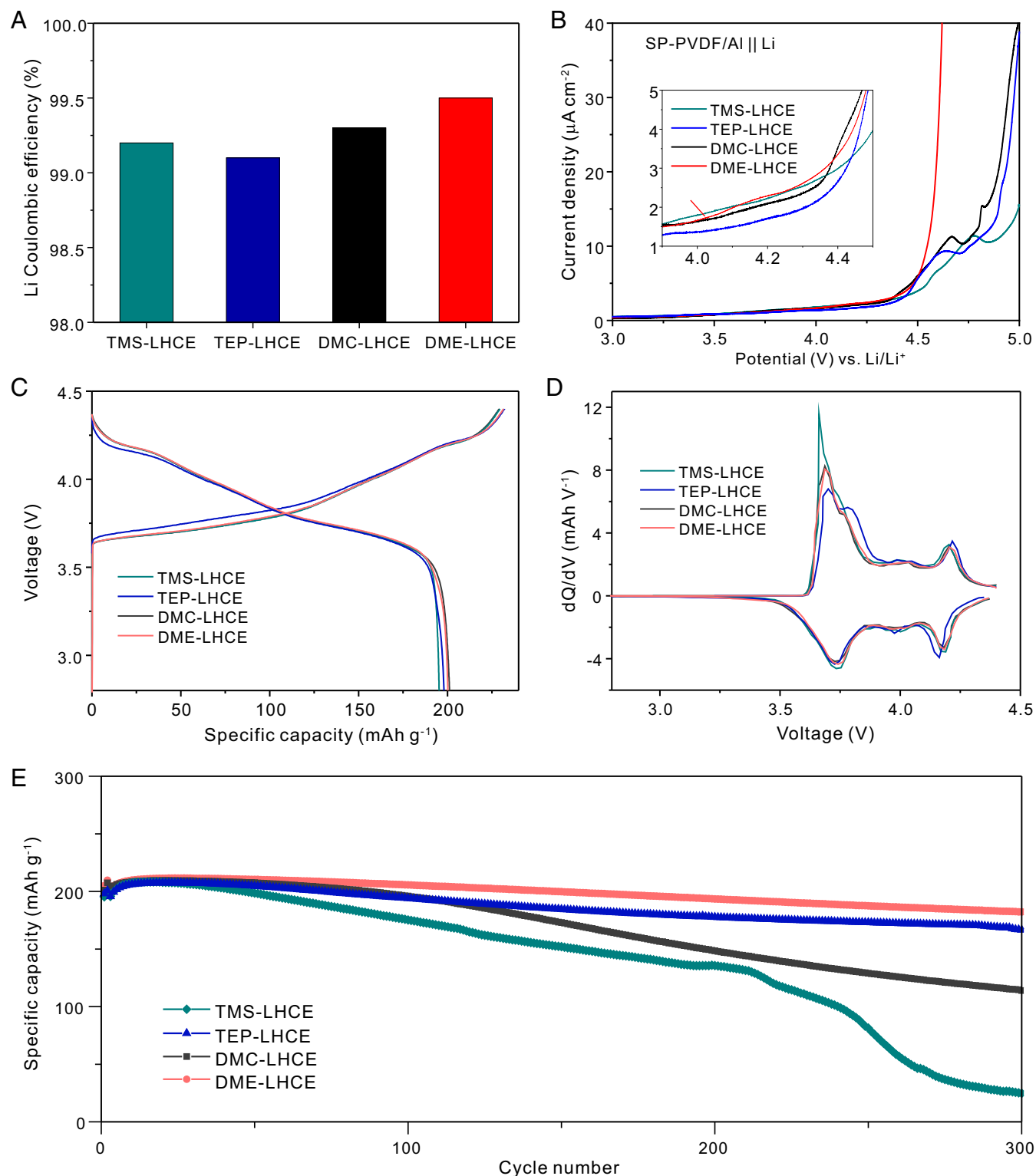
Fig. 3. (*A*) Average Li CEs measured in Li||Cu cells using different LHCEs. (*B*) Oxidation stabilities of LHCEs on SP-PVDF/Al electrode. (*C*) Voltage-capacity profiles of the first formation cycle of Li||NMC811 cells using different LHCEs at C/10 rate in the voltage range of 2.8–4.4 V. (*D*) The corresponding dQ/dV curves of the first formation cycle of Li||NMC811 cells with the four LHCEs. (*E*) Comparison of cycling performances of Li||NMC811 cells using different LHCEs in the voltage range of 2.8–4.4 V at C/3 charge/discharge rates after two formation cycles at C/10 rate.

clear porous surface layers on top of Li anodes (*SI Appendix*, Fig. S5), which result from accumulated side-reaction products between Li metal and electrolytes. While the DMC-LHCE shows a high Li CE of 99.3% from the 10-cycle CE measurement, the Li

corrosion layer (i.e., the porously structured surface layer on Li) has the highest average thickness of 60.3 μm, which is undesirable for efficient Li$^+$ diffusion. In contrast to the faster corrosion layer buildup in the DMC-LHCE (60.3 μm) and the TEP-LHCE

(~51.8 μm), much thinner corrosion layers are seen in the TMS-LHCE (~40.0 μm) and the DME-LHCE (~40.5 μm) along with limited increase in Li$^+$ diffusion resistance. Meanwhile, the least change of the charge-transfer resistance is found in the TEP-LHCE, in agreement with the high-cell CE shown in *SI Appendix,* Fig. S2. Since only limited changes of the bulk crystalline structure of the cathodes can be found by X-ray diffraction (XRD) after 100 cycles (*SI Appendix,* Fig. S6), the cell degradations can be mainly attributed to the evolutions of the electrode/electrolyte interphases. To better illustrate the relationship between coordinating solvents in LHCEs and the electrode/electrolyte interfacial chemistries, the Li/electrolyte and the NMC811/electrolyte interphases will be discussed separately in the following two sections.

Li/Electrolyte Interphase. In recent studies, various LiFSI-based HCEs and LHCEs have been used in LMBs and demonstrated greatly improved Li metal stability compared to conventional LiPF$_6$-based electrolytes (16, 18, 34). In contrast to dendritic Li growth, very similar nodulous Li metal deposits can be grown on

Cu substrates in those electrolytes. This change was believed to be related to the formation of LiF-enriched SEI layer derived from the LiFSI salt. Nevertheless, little attention have been paid to the role of the solvents. Here, X-ray photoelectron spectroscopy (XPS) analysis was carried out to characterize the Li anode SEI layers formed in different LHCEs. Special care was taken to avoid exposing the XPS samples to ambient atmosphere during sample transportation and loading.

As shown in Fig. 4, the similar F 1s and S 2p spectra agree with our expectation that the reduction of the LiFSI salt is critical for stabilizing the Li metal. However, the top SEI layers consist of many Li and O elements along with intermediate amount of C element, compared to the relatively small ratios of F, S, and N elements. This suggests that the solvating solvent molecules also make a great contribution in the SEI layers. Although the similar elemental compositions make it difficult to draw an unambiguous conclusion, the high atomic ratio of O could be evidence indicating the decomposition of solvent molecules in the SEI formations. If we assume that the TTE diluent has the same reactivity on
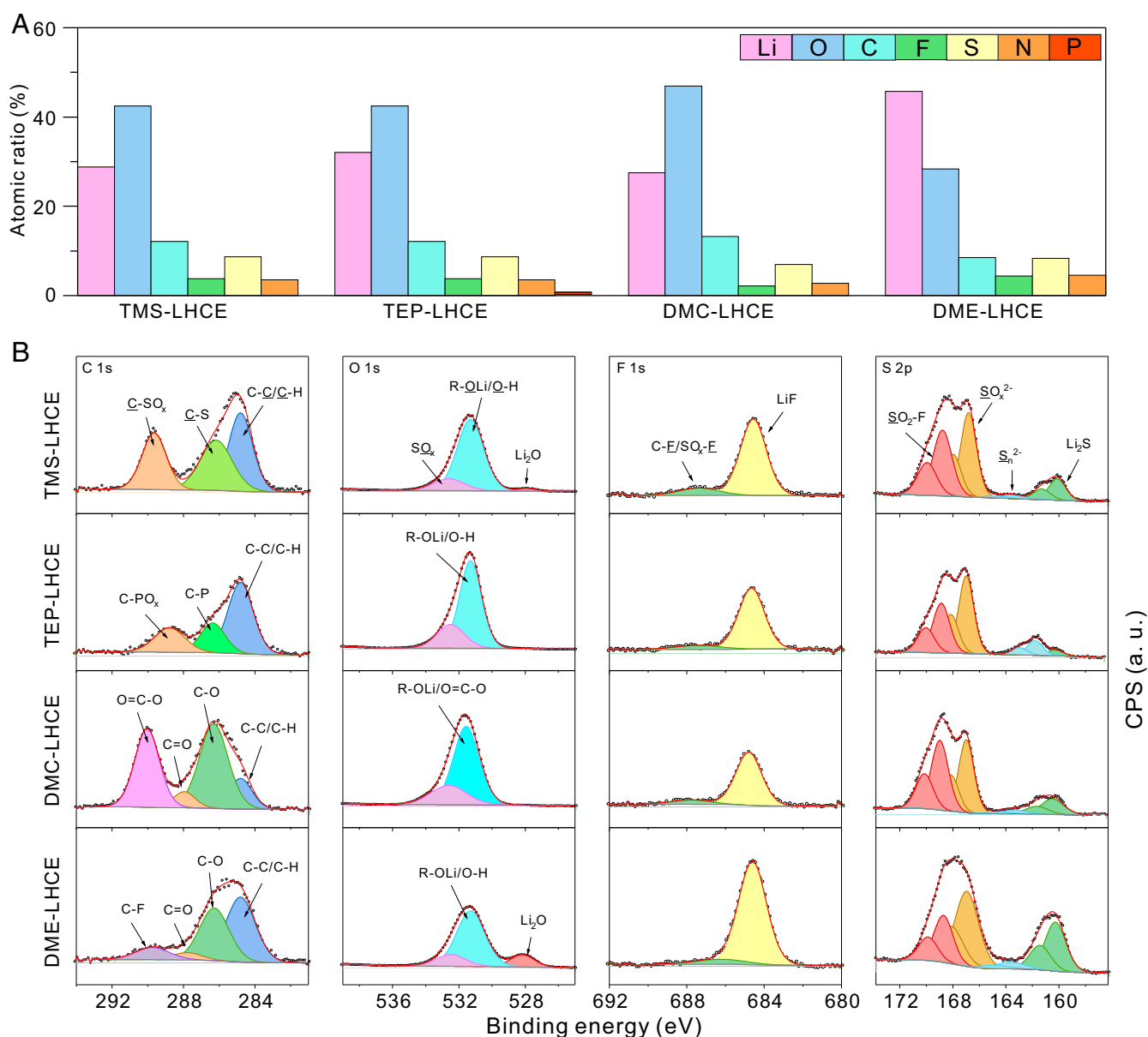

Fig. 4. (*A*) XPS atomic ratios of different elements on cycled Li anodes using different LHCEs. (*B*) XPS spectra for selected elements on cycled Li anodes.

the Li metal in these LHCEs, the ratios between the C atoms and the Li atoms can be used to compare the reaction tendency of different solvent molecules on the Li anode, which follows the order as: DMC (0.48) > TMS (0.42) > TEP (0.28) > DME (0.19). In addition, the C 1s and O 1s spectra in the DMC-LHCE (Fig. 4B) exhibit signals with slightly higher binding energies (C 1s, 290.0 eV; O 1 s, 531.6 eV) than the other three samples, which is likely to be O−C=O species from DMC molecules. Albeit the atomic ratio of P in the TEP-LHCE sample is small, it also supports the decomposition of TEP molecules during the SEI formation (*SI Appendix*, Fig. S7C), considering some partially reduced TEP molecules may tend to dissolve into the electrolyte. Such variations of compositions and structures of the Li surface layers due to the participation of solvent molecules in the reactions have a close relationship with the Li$^+$ ion transport and Li metal plating/stripping behaviors, as shown before. Among the four LHCEs studied, the ether-based LHCE, in which the DME molecules are more stable against Li metal, demonstrates the highest Li CE and the least surface-layer buildup after cycling. In addition to the apparently higher F and N and lower C atomic ratios in the DME-LHCE samples than those in the other samples, the more apparent Li$_3$N signal from the N 1s spectrum (396.1 eV, *SI Appendix*, Fig. S7A) and the Li$_2$O signal from the O 1s spectrum (528.2 eV, Fig. 4B) also suggest the inhibited DME decomposition and the preferred reduction of LiFSI are highly beneficial for enhancing the LMA stability.

Cathode/Electrolyte Interphase. Compared to the effects of solvating solvent molecules on the LMA stability in the LHCEs, their effects on the Ni-rich NMC811 cathode are even more dramatic. As shown in Fig. 3E, the selected solvents largely determined the stability of cathode and the cycling performance of cells, where the differences in the stability of LMA are minimized by the excess amount of Li metal and electrolyte. Despite the good oxidation stability of most of the solvents selected (DMC, TEP, and TMS), which would be further enhanced with high salt/solvent ratios in LHCEs, solvent molecules are found to be critical in the interfacial reactions on the Ni-rich NMC811 during charging (up to 4.4 V). As shown by the XRD patterns of the NMC811 cathodes after 100 cycles in the four different LHCEs in *SI Appendix*, Fig. S6, except for the minor shifts of the (003) and (108)/(110) reflections for the cathode samples cycled in TMS-LHCE, TEP-LHCE, and DMC-LHCE from the pristine one, the main crystalline structures of cycled NMC811 cathodes show negligible changes, indicating the relative structural integrity of the NMC8111 after cycling. Specifically, the NMC811 cathode from DME-LHCE does not show even the minor shifts in both (003) and (108)/(110) reflections (*SI Appendix*, Fig. S6 B and C), demonstrating the well-maintained crystalline structure of the cathode by this electrolyte.

Comparing the top-view SEM images of the cathodes after 100 cycles to that of the pristine cathode (Fig. 5 A–D and *SI Appendix*, Fig. S8), the accumulations of electrolyte decomposition products and the evolutions of the secondary particle structures could be found. The population of cracked particles follows the sequence from high to low as TMS-LHCE > DMC-LHCE > TEP-LHCE > DME-LHCE. In addition, the cross-sections of the cycled cathodes prepared using focused ion beam (FIB) cut method also exhibit the propagation of cracking inside the secondary particles and follow the same order in cracking amount (Fig. 5 E–H). It is likely that the anisotropic volume expansion of primary particles during charge and discharge processes will enlarge the gap between them and induce side reactions between the cathode and the electrolyte. If the CEI layer from the initial cycles in an electrolyte cannot well passivate the cathode particles, the side reactions cannot be stopped; then, the gap among the primary particles will be further increased and the cracks will grow toward the inner side of the secondary particle and break

the contact between primary particles. The tendency of the secondary particle stability could partially explain the cycling performance of the Li||NMC811 cells with the four LHCEs, in the order from high to low as DME-LHCE > TEP-LHCE > DMC-LHCE > TMS-LHCE as shown in Fig. 3E.

Furthermore, the cathodes after 100 cycles were characterized by annular bright-field scanning transmission electron microscopy (ABF-STEM) and high-angle annular dark-field (HAADF)-STEM to study the effect of different LHCEs on the CEI, as shown in Fig. 5 I–L. The HAADF-STEM is used to show the distribution of atoms, which are transition-metal ions, in Z-contrast images. In the TMS-LHCE, the surface of the cathode particle developed a thick yet irregular layer (~5.7 nm) with disordered rock-salt or cation-mixing phase structure (Fig. 5I). This phase transformation from the initial layered R-3m structure is likely caused by the formation of corrosion products from the side reactions between the cathode surface and the electrolyte and the resulting dissolution of transition-metal ions. Because of the limited free-solvating solvent molecules in the LHCE, the dissolved metal ions tend to precipitate on the cathode surface. In the DMC-LHCE, a relatively thinner layer (2.3 nm) with phase change was observed (Fig. 5K), but there are signals from transition-metal ions in the thick layer on top, suggesting apparent cathode corrosion by this electrolyte. For the other two LHCEs based on TEP (Fig. 5J) and DME (Fig. 5L), the cation-mixing layers are much less significant. The variation of the transformed layer thicknesses in the four LHCEs (5.7 nm in TMS-LHCE, 2.3 nm in DMC-LHCE, 1.4 nm in TEP-LHCE, and 1.0 nm in DME-LHCE) agrees with the cell capacity decay trend shown in Fig. 3E.

On the other hand, the ABF-STEM images, which visualize both light and heavy elements, can tell different features of the outer surfaces of the cathode particles. As shown in Fig. 5 M–P, the interfacial layers from different cathode-electrolyte reactions can be clearly seen. Apart from the TMS-LHCE sample with severe cathode corrosion, the CEI layer formed in the DMC-LHCE is the thickest (4.3 nm) yet mostly amorphous, which may explain its poor ability to protect the cathode from electrolyte corrosion. Among the four LHCEs studied, the DME-LHCE leads to the thinnest CEI and the least phase change, which further proves the superior capability of the ether-based LHCE for stabilizing Ni-rich NMC811 under the high voltage of 4.4 V. Although the TEP-LHCE induces a more apparent degradation at the interphase than that of the DME-LHCE, it also results in not severe cracks in secondary particles, which may account for the small change of the charge-transfer resistance shown in *SI Appendix*, Fig. S4F.

To further study the interactions between the LHCEs based on different solvating solvents and the Ni-rich cathode and to understand the interfacial chemistry, the surface layers of the NMC811 cathodes after 100 cycles were characterized by XPS. Fig. 6A compares the atomic ratios of Li, F, C, O, S, and N of the cathodes cycled in different LHCEs and their regional spectra are shown in Fig. 6B and *SI Appendix*, Fig. S9. Compared to the pristine NMC811, which shows signals from the conductive carbon, the PVDF binder, and the surface carbonate/oxide layer, the cycled cathode surfaces exhibit apparent changes due to reactions with electrolytes. The increases in atomic ratios of Li, F, S, and N, as well as the evolutions of LiF (684.7 eV) in F 1s spectra and higher-valence S species (e.g., SO_4^{2-} at 169.0 eV, S 2p$_{3/2}$) are pointing to the reactions of the LiFSI salt on the cathodes. The lower C atomic ratios and the weaker signals from C 1s spectra compared to those of the pristine NMC are likely due to the accumulated electrolyte reaction products on the cathodes (particularly the conductive carbon). The significant amount of LiF (Li: 40.2%, F: 43.4%) found on the cathode surface from the DME-LHCE supports previous discussions (14, 18) about the critical role of LiF at an appropriate amount in the
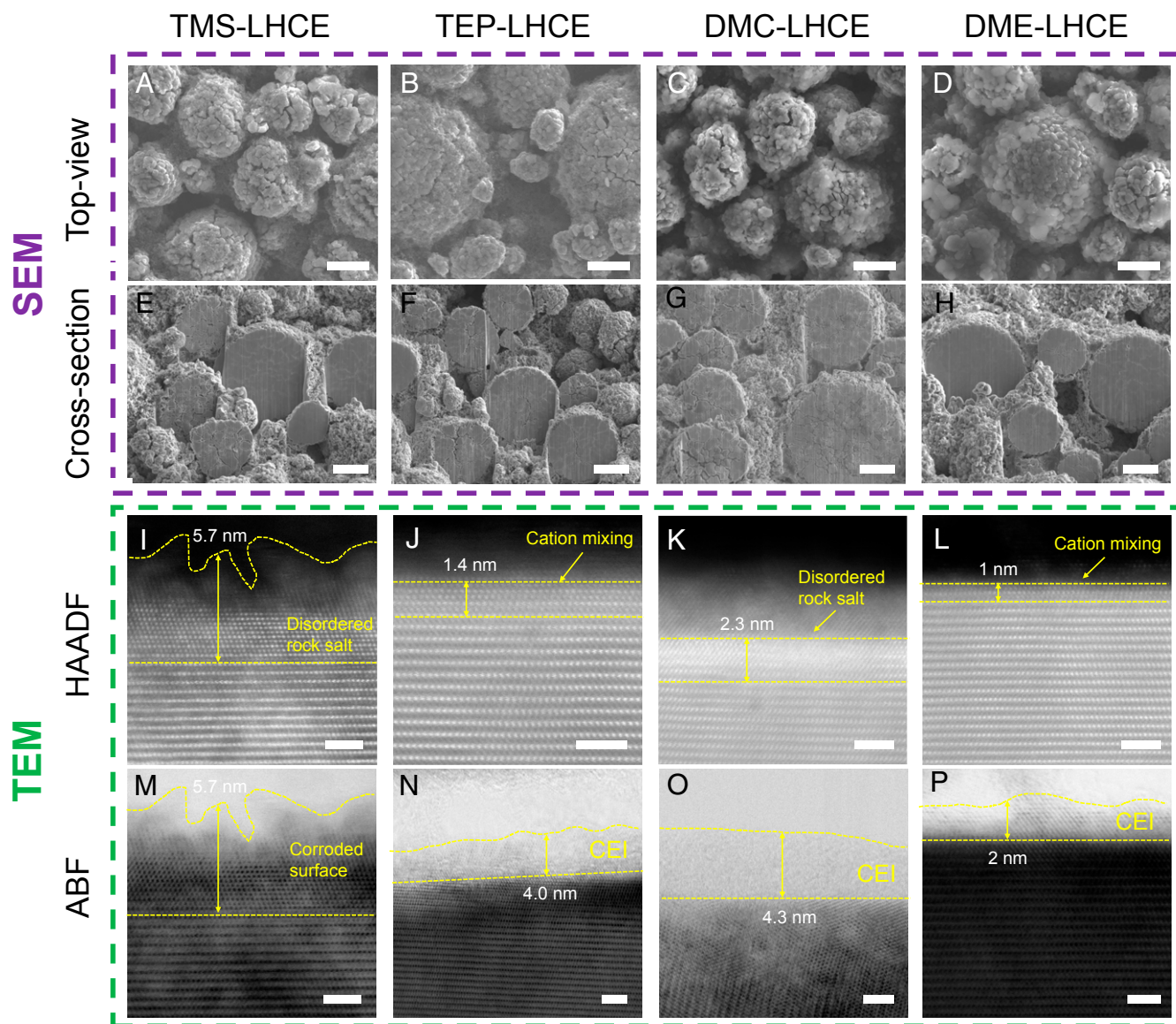
Fig. 5. Electron microscopic characterizations of cycled NMC811 cathodes in different LHCEs. (*A–D*) Top-view SEM images, (*E–H*) cross-section SEM images, (*I–L*) HAADF-STEM images, and (*M–P*) ABF-STEM images [Scale bars, (*A–H*) 5 μm, (*I–P*) 2 nm.]

electrode/electrolyte interphase for effective interfacial protection. With the protection of this LiF-enriched CEI from the DME-LHCE, no apparent M-O signal due to transition-metal dissolution can be seen in the O 1s spectrum (Fig. 6*B*) and the cathode structure is well maintained (Fig. 5 *H, L*, and *P* and *SI Appendix*, Fig. S6).

Despite the high LiF content found on the NMC811 sample from the DMC-LHCE, the poor crystallinity of the CEI cannot prevent the penetration of the electrolyte and effectively protect the cathode. It is interesting to note in the TEP-LHCE that although the ratios of Li, F, S, and N are relatively lower compared to the other samples and the LiF ratio in the F 1s spectrum is significantly smaller, its cycling stability is only inferior to that in the DME-LHCE. This suggests that the LiFSI salt has the least tendency to react on the cathode when coordinating with TEP molecules compared to others, which explains its dQ/dV difference (Fig. 3*D*). The relatively stable cell cycling in the TEP-LHCE could also partially be attributed to the PO_4^{3-} species formed in the CEI, as demonstrated in the XPS P 2p spectrum (*SI Appendix*, Fig. S9). Both LiF and PO_4^{3-} species can also limit

the electrolyte side reactions between the NMC811 and the TEP-LHCE, which is also evidenced by its highest cell CE (99.9%). As for the NMC811 cycled in the TMS-LHCE, the feature (e.g., $C-SO_x^{2-}$, S = O) in the S 2p spectrum indicates TMS molecules are involved in the cathode–electrolyte reactions, which also accounts for the accelerated cathode decay and poor cell cycling performance.

Simulations on Electrolyte Systems. To elucidate the interfacial reaction mechanism, ab initio molecular-dynamics (AIMD) simulations were performed to the electrolyte systems of LiFSI and TTE with different solvating solvents (DMC, TMS, TEP, and DME). *SI Appendix*, Fig. S10 shows the projected density of states (PDOS) plots of LiFSI salt with various solvents in diluent TTE obtained by AIMD simulations. It is found that the valence band maxima (HOMO energy levels) of the electrolytes are all on the solvating solvents, which means the solvents are easy to be oxidized on cathode. While this result is consistent with the intuitive understanding of conventional electrolytes, it could not satisfactorily explain the reactivity trend of different LHCEs on
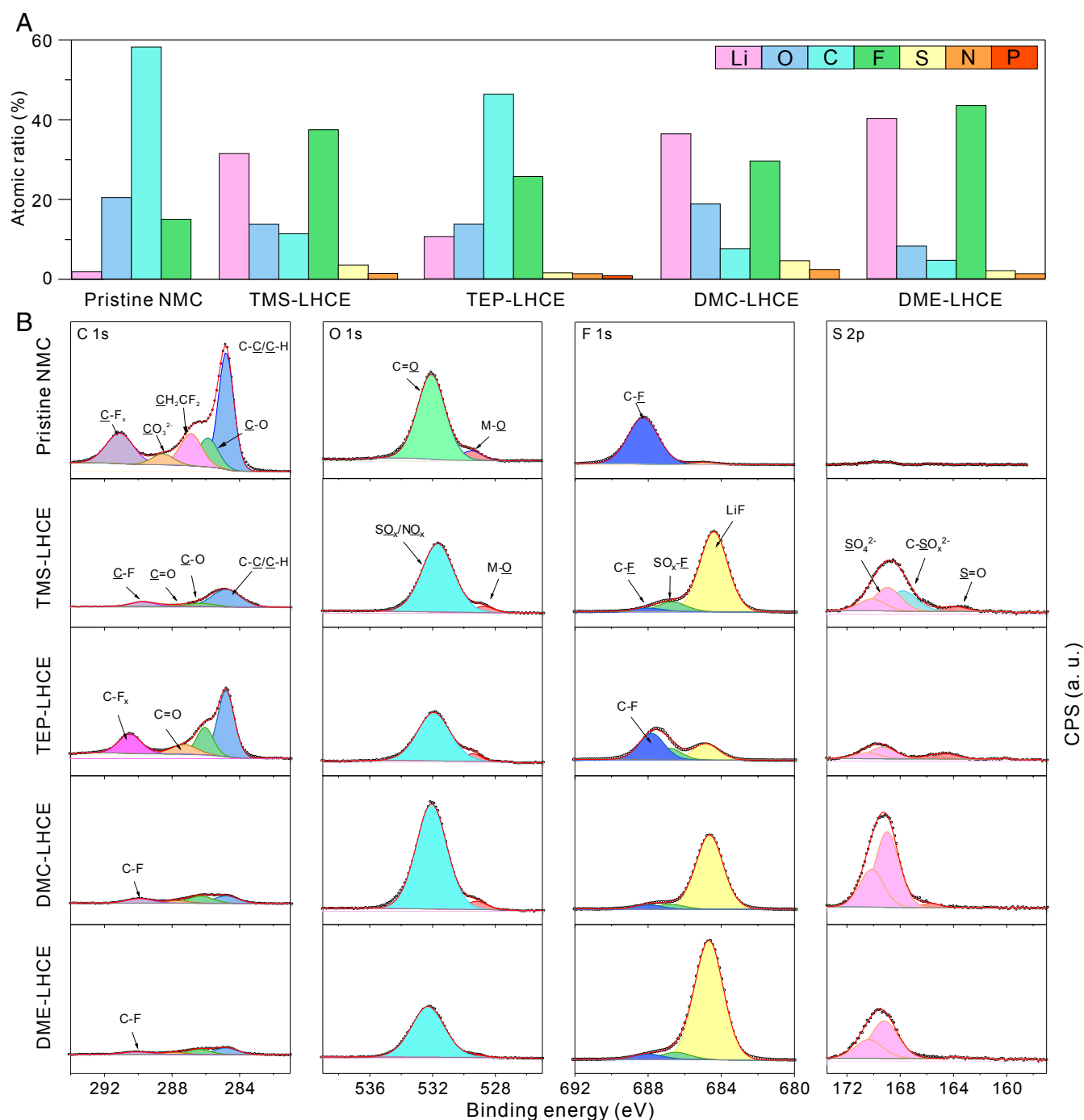
APPLIED PHYSICAL SCIENCES

Fig. 6. (*A*) Atomic ratios of different elements measured by XPS on cycled NMC811 cathodes using different LHCEs. (*B*) XPS spectra of selected elements for cycled NMC811 cathodes.

the cathode. It is worth noting that the AIMD simulation is limited to a short timescale of tens of picoseconds due to calculation capacity, which is unable to capture essential reaction processes happening on longer timescales, for example, the proton transfer (H-transfer) reactions between the solvent and the anion or diluent. Nonetheless, such anodic reaction pathways on the cathode surface are highly likely for common LIB electrolyte components (35).

To better understand the formation mechanism of CEI, additional density-functional theory (DFT) calculations were performed to study the effect of H-transfer reactions between solvent and anion/diluent on cathode. Various individual species

and complexes with potential interactions in the LHCEs were taken into consideration in the DFT calculations and their oxidation potentials are shown in Fig. 7*A*. For individual species, the oxidation potential of the diluent molecule (TTE) is the highest, wherever that of the FSI⁻ anion is the lowest, except that the DME solvent molecule has a lower oxidation potential than the FSI⁻ anion. While the behavior of individual species cannot explain the reaction features of different LHCEs, the interactions in molecular complexes are believed to greatly influence the reaction landscape on the cathode. Compared to the individual species, the oxidation potentials of their molecular complexes decrease significantly, with

those of the solvent–anion complexes as the lowest ones, where H-transfer reactions are taking place between solvent and FSI⁻ anion (N atom as the preferred proton acceptor).

The optimized structures of those H-transfer reactions are shown in Fig. 7B, where the red arrows and dotted circles indicate the active sites. Because of the highly electrophilic S center in FSI⁻, subsequent nucleophilic substitution by reaction intermediators could drive the leaving of F⁻ and the formation of LiF in the CEI (36). The trend of decreasing amount of LiF contents on the cathodes in four LHCEs (Fig. 6A, DME-LHCE > TMS-LHCE > DMC-LHCE > TEP-LHCE) is found to be generally in correlation with the increasing of calculated oxidation potentials of the solvent–anion complexes. Although specific interactions between catalytically active cathode surface and electrolyte components, and the influences of other possible corrosive side products are not included in the DFT calculation, charge-transfer reactions in the inner solvation sheath of LHCEs provide a critical perspective in understanding the solvation chemistry and its functioning mechanism on electrodes. In our previous study (26), it was indicated that the diluent also participated in the CEI formation chemistry, yet the detailed mechanism was unclear at that time. The calculations in this work also show that the oxidation potentials of anion–diluent and solvent–diluent complexes decrease when the H-transfer reactions occur, and the optimized structures of solvent–diluent complexes with H transfer at oxidation state are also shown in *SI Appendix*, Fig. S11. However, their higher oxidation potentials than anion–solvent complexes imply that the contribution of solvent–diluent or anion–diluent complexes to the F components in CEI would be relatively small compared to the solvent–anion complexes.

The PDOS analysis also shows that the conduction band minima (LUMO energy levels) are all on the FSI⁻ anions in the LHCEs, implying the FSI⁻ anions are predominantly reduced on the Li anode, which agrees with the aforementioned results that the FSI⁻-derived SEI layer is highly beneficial for enhancing the LMA stability. Nevertheless, this fails to justify the effect of different solvents on the Li anode/electrolyte chemistry. To understand the mechanism behind this discrepancy, the charge-transfer reaction is also considered in our study via DFT calculations.

Fig. 7C shows the reduction potentials of solvation clusters and individual solvent/diluent/anion. The proportion of molecules in clusters is following the molar ratios listed in *SI Appendix*, Table S1. Limited to the computational power, only one or two Li⁺ ions were included in the clusters. For the reduction of individual molecule/anion, it is shown that FSI⁻ anion is easier to be reduced, which agrees with AIMD simulation result. Besides, the reduction potential of TTE is very close to FSI⁻, implying TTE might be reduced on anode as well. It is interesting to find out that the reduction potentials of solvent–salt complexes decrease compared to individual species, indicating the solvent or FSI⁻ anion in clusters is actually more electrochemically stable against reduction in the inner solvation sheath of LHCEs. As a result, the reductions of salt–solvent clusters are accompanied by charge transfer between FSI⁻ anion and solvent, highlighting the roles of both anion and solvent in the SEI formation process. It should be noted that for the LiFSI-DME and LiFSI-TEP clusters, the S–N bond length (original value 1.56 Å) is stretched to 3.40 and 3.10 Å after the complexes accept one electron, indicating the favorable S–N bond breaking before solvent decomposition, which is consistent with solvent reactivity trend on Li metal from XPS analysis. Further reactions with solvent molecules to generate LiF [e.g., F-transfer reaction in LiFSI-DME reduction, as in previous DFT calculations by Kim et al. (37)] and other components observed in the SEI may be alternative pathways during SEI formations. The reason for the low Li CE measured in the TEP-LHCE is unclear right now, but is possibly related to "dead" Li loss during Li stripping.

From the above experimental and computational results, we see that the chemical nature of the Li salt and the solvent molecule and their intimate interactions in the inner solvation sheath of the LHCE have tremendous effects on the interfacial chemistries between the anode or cathode and the electrolyte. Instead of individual salt and solvent molecules, the salt–solvent clusters as a whole and their proton/charge-transfer processes, are controlling the chemical compositions and the structures at both the cathode/electrolyte and the anode/electrolyte interphases. For the DME-LHCE, where the H-transfer between DME and LiFSI is most likely to happen in the anodic process, a CEI layer enriched in LiF can be formed effectively to protect the NMC811 cathode. On the other hand, it is so difficult for the H-transfer
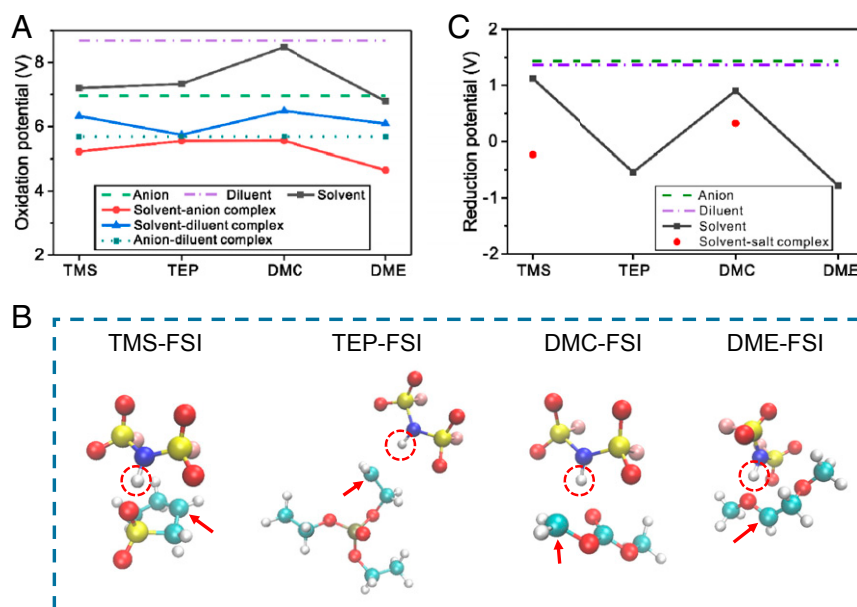
Fig. 7. (*A*) Comparison of oxidation potentials of various molecules and complexes. (*B*) The snapshots of anion–solvent complexes with H-transfer reactions. (*C*) Comparison of reduction potentials of various molecules and complexes. Note that the reduction potentials of LiFSI-DME and LiFSI-TEP are not shown because the decompositions of FSI⁻ anions in these two clusters were observed.

reaction in the TEP-LHCE to happen that reactions involving LiFSI are very limited on the cathode. For the DMC-LHCE, the participations of DMC in both the CEI and the SEI reaction processes have negative effects on the electrode stabilities, with unsatisfactory cathode protection and thick anode surface layer buildup. On the contrary, the synergistic interactions between DME and LiFSI in the DME-LHCE have enabled the best performances on both the NMC811 cathode and the LMA.

Conclusions

In this work, a series of LHCEs with four different model solvent molecules (carbonate, sulfone, phosphate, and ether) are investigated in high-voltage Li∥NMC811 cells. Electrochemical tests and electron microscopies show largely different cathode/electrolyte and anode/electrolyte stabilities with the solvents selected. Among the four LHCEs, the DME-LHCE demonstrates the best capabilities to stabilize both the LMA and the Ni-rich cathode. XPS analysis proves both the salt and the solvent in the LHCEs are involved in the reactions at the electrode/electrolyte interfaces. Further theoretical analysis reveals that the strong interactions between the salt and the solvent in the inner solvation sheath of the LHCEs greatly influence their individual reactivities. Their intermolecular proton/charge-transfer processes are likely the key steps for the interfacial reactions. This work provides crucial insights in understanding the electrolyte solvation structure and its implications on the electrode/electrolyte interfacial chemistry. We hope these findings will stimulate critical thinking for rational electrolyte design for not only high-voltage LMBs, but also other electrode materials and battery systems.

Materials and Methods

Materials. LiFSI (battery grade, Nippon Shokubai) was dried under vacuum at 120 °C for 24 h before use. DME and DMC (both in battery grade) were purchased from Gotion and used as received. TMS (99%, Sigma-Aldrich) was further purified by distillation under vacuum and then dried with 4A molecular sieves before use. TEP (99.8%, Sigma-Aldrich) and TTE (99%, SynQuest Laboratories) were dried with preactivated molecular sieves before use. Li metal chips (thickness: 450 μm, diameter: 15.5 mm) were ordered from MTI Corporation. Ni-rich NMC811 material (SNMC-03008) was ordered from Targray. To prepare the cathode laminates, slurry coating using NMC811 material, conductive carbon (C-NERGY Super P C65, Timcal), and PVDF binder (Kureha L#1120) with a weight ratio of 96:2:2 was used. Cathode disks had a diameter of 1.27 cm and the loading was about 1.5 mAh cm^{-2}.

Electrolyte Preparation. To prepare the LHCEs, LiFSI salt and TTE diluent were first mixed together in a glass vial with a molar ratio of 1:3. As LiFSI can barely be dissolved in TTE, the mixture has white solid suspensions. Under stirring, the main solvent (e.g., DMC, TEP, TMS, or DME) was added dropwise into the suspension using a micropipette. The salt saturation point was determined when the white salt particles in the suspension disappeared and the solution became clear. Then another 5% (by volume) of the total amount of the main solvent previously used was added into the solution to prevent precipitation of salt–solvent clusters during cell cycling.

Electrochemical Tests. For coin cell tests, CR2032-type (MTI) cells were assembled inside an argon-filled glovebox (MBraun, H_2O < 1 ppm, O_2 < 1 ppm). Li foil, polyethylene (PE) separator (Asahi Kasei), and cathode disk were sandwiched together to make a Li∥NMC811 cell. Into each coin cell, 75 μl of electrolyte was added. To prevent the corrosion of the stainless-steel positive case, Al-clad positive one (a positive case made by stainless-steel 304 with Al coating) was used (EQ-CR2032-CASE-AL, MTI). An additional Al foil was placed in between the cathode disk and the Al-clad case. Previous studies have demonstrated greatly improved Al stability under high voltages in HCEs and LHCEs. (22, 24) Galvanostatic cycling was performed within the voltage window of 2.8–4.4 V using Landt battery testers (Wuhan Land) inside a temperature chamber (TestEquity) at 25 °C. The first two formation cycles were carried out at a C/10 charge/discharge rate and then the cells were charged to 4.4 V at C/3 and held at 4.4 V until the anodic current dropped below C/20 before discharged to 2.8 V at C/3.

Characterizations. For postanalyses on the samples, the coin cells after cycling were disassembled inside the glovebox and rinsed several times with anhydrous solvents to remove residual electrolytes before vacuum drying. XRD patterns were obtained on a Rigaku MiniFlex II XRD instrument (Cu K_a radiation, 30 kV, 15 mA, and scan rate 0.3°/min). Processing of samples for cross-sectional imaging and TEM preparation was performed on an FEI Helios Nanolab 660 Dualbeam Ga FIB SEM. Cross-sections cut to expose the core of particles were done with the ion beam at an accelerating voltage of 30 kV and a current of 2.5 nA with a polish at 0.43 nA. TEM samples were prepared by first laying 300 nm of electron-beam-deposited Pt and 3 μm of ion-beam-deposited C to protect the sample from Ga-ion damage, then following standard lift-out procedures. Thinning was performed with the ion beam at 30 and 5 kV, and a final polish was applied at 2 kV to reduce the amorphous damage layer. Other characterizations, e.g., XPS, SEM, and TEM, were carried out following the same procedures as described in our previous work (26). The electrode samples were retrieved from the cycled coin cells, washed, dried, and then sealed in the airtight containers in the argon-filled glovebox in our laboratory. The samples were transferred into another glovebox attached to the XPS instrument. Inside the second glovebox filled with inert gas, the electrode samples were taken out of the airtight container, mounted on the sample holder, and then transferred into the XPS instrument. Therefore, the samples were never exposed to the ambient air during sample preparation, transportation, and loading process.

Simulation Details. DFT calculations were performed using the M06-HF functional with NWCHEM software. The M06-HF functional was selected as it is a suitable option to capture the charge-density differences of anion–solvent complexes in a physically consistent way (38, 39). The initial structures of complexes were extracted from classical molecular-dynamics simulation with COMPASS force field by simulated annealing algorithm (40). Then the geometry of the molecules/complexes was further optimized with 6–31G* basis(6-31+G* for anion). Single-point energy calculations were performed using 6–311++G(d,p) basis set. Vibrational frequencies were calculated for yielding zero-point energy and thermal corrections. Gibbs free energies were calculated at 298.15 K. An effect of implicit solvent with dielectric properties of TTE (dielectric constant = 6.2) was included via COSMO model. The oxidation potential E_{ox} vs. Li/Li$^+$ was calculated as follows:

$$E_{ox} = \frac{G(M^+) - G(M)}{F} - 1.4\ V,$$

$$E_{red} = \frac{G(M) - G(M^-)}{F} - 1.4\ V,$$

where $G(M)$, $G(M^+)$, and $G(M^-)$ are the free energy of species M, its oxidized and reduced forms at 298.15 K, respectively. F is the Faraday constant. AIMD simulations were carried out by Vienna Ab initio Simulation Package (VASP). Electron–ion interactions were described by the projector-augmented wave pseudopotentials (41) with the cutoff energy of 400 eV. The exchange-correlation functional was represented using the Perdew–Burke–Ernzerhof generalized gradient approximation. The exchange-correlation functional with a Gaussian smearing width term of 0.05 eV was used. The convergence criterion for electronic self-consistent iteration was set to 1 × 10^{-5} eV. The effects of solvent on the microscopic structures were investigated using AIMD simulations in the canonical ensemble at 298.15 K. The constant temperature of the AIMD simulation systems was controlled using the Nosé thermostat method with a Nosé-mass parameter of 0.1. The initial structure of each LiFSI salt/solvent/diluent mixture system was set up by randomly placing the numbers of solvent (DME, TEP, DMC, or TMS), diluent (TTE), and LiFSI molecules on the basis of experimental densities and molar ratios. These initial structures were firstly optimized with molecular mechanics and molecular-dynamics method with COMPASS force field (36). A time step of 1 fs was used in all AIMD simulations. A Monkhorst–Pack k-point mesh grid scheme was 2 × 2 × 2. The systems were preequilibrated for 5 ps. Then, the production time was 10 ps. Ten structures from the trajectory were selected and averaged to calculate the PDOS.

Data Availability. All study data are included in the article and *SI Appendix*.

1. W. Xu et al., Lithium metal anodes for rechargeable batteries. *Energy Environ. Sci.* **7**, 513–537 (2014).
2. X. B. Cheng, R. Zhang, C. Z. Zhao, Q. Zhang, Toward safe lithium metal anode in rechargeable batteries: A review. *Chem. Rev.* **117**, 10403–10473 (2017).
3. D. Lin, Y. Liu, Y. Cui, Reviving the lithium metal anode for high-energy batteries. *Nat. Nanotechnol.* **12**, 194–206 (2017).
4. A. Manthiram, J. C. Knight, S. T. Myung, S. M. Oh, Y. K. Sun, Nickel-rich and lithium-rich layered oxide cathodes: Progress and perspectives. *Adv. Energy Mater.* **6**, 1501010 (2016).
5. J. Liu et al., Pathways for practical high-energy long-cycling lithium metal batteries. *Nat. Energy* **4**, 180–186 (2019).
6. K. Xu, Electrolytes and interphases in Li-ion batteries and beyond. *Chem. Rev.* **114**, 11503–11618 (2014).
7. J. Li, L. E. Downie, L. Ma, W. Qiu, J. R. Dahn, Study of the failure mechanisms of Li-Ni0.8Mn0.1Co0.1O2 cathode material for lithium ion batteries. *J. Electrochem. Soc.* **162**, A1401–A1408 (2015).
8. H.-H. Ryu, K.-J. Park, C. S. Yoon, Y.-K. Sun, Capacity fading of Ni-rich Li[NixCoyMn1–x–y]O2 (0.6 ≤ x ≤ 0.95) cathodes for high-energy-density lithium-ion batteries: Bulk or surface degradation? *Chem. Mater.* **30**, 1155–1163 (2018).
9. X. Ren et al., Guided lithium metal deposition and improved lithium coulombic efficiency through synergistic effects of LiAsF6 and cyclic carbonate additives. *ACS Energy Lett.* **3**, 14–19 (2017).
10. Z. Zhu et al., Fluoroethylene carbonate enabling a robust LiF-rich solid electrolyte interphase to enhance the stability of the MoS2 anode for lithium-ion storage. *Angew. Chem. Int. Ed. Engl.* **57**, 3656–3660 (2018).
11. Y. Jie et al., Enabling high-voltage lithium metal batteries by manipulating solvation structure in ester electrolyte. *Angew. Chem. Int. Ed. Engl.* **59**, 3505–3510 (2020).
12. J. M. Zheng et al., Electrolyte additive enabled fast charging and stable cycling lithium metal batteries. *Nat. Energy* **2**, 17012 (2017).
13. X. Li et al., Dendrite-free and performance-enhanced lithium metal batteries through optimizing solvent compositions and adding combinational additives. *Adv. Energy Mater.* **8**, 1703022 (2018).
14. X. Fan et al., Non-flammable electrolyte enables Li-metal batteries with aggressive cathode chemistries. *Nat. Nanotechnol.* **13**, 715–722 (2018).
15. Y. Jie, X. Ren, R. Cao, W. Cai, S. Jiao, Advanced liquid electrolytes for rechargeable Li metal batteries. *Adv. Funct. Mater.* **30**, 1910777 (2020).
16. J. Qian et al., High rate and stable cycling of lithium metal anode. *Nat. Commun.* **6**, 6362 (2015).
17. X. Fan et al., Highly fluorinated interphases enable high-voltage Li-metal batteries. *Chem* **4**, 174–185 (2018).
18. L. Suo et al., Fluorine-donating electrolytes enable highly reversible 5-V-class Li metal batteries. *Proc. Natl. Acad. Sci. U.S.A.* **115**, 1156–1161 (2018).
19. J. Wang et al., Superconcentrated electrolytes for a high-voltage lithium-ion battery. *Nat. Commun.* **7**, 12032 (2016).
20. S. H. Jiao et al., Stable cycling of high-voltage lithium metal batteries in ether electrolytes. *Nat. Energy* **3**, 739–746 (2018).
21. Y. Yamada, J. Wang, S. Ko, E. Watanabe, A. Yamada, Advances and issues in developing salt-concentrated battery electrolytes. *Nat. Energy* **4**, 269–280 (2019).
22. X. Ren et al., High-concentration ether electrolytes for stable high-voltage lithium metal batteries. *ACS Energy Lett.* **4**, 896–902 (2019).
23. S. Chen et al., High-voltage lithium-metal batteries enabled by localized high-concentration electrolytes. *Adv. Mater.* **30**, e1706102 (2018).
24. X. Ren et al., Localized high-concentration sulfone electrolytes for high-efficiency lithium-metal batteries. *Chem* **4**, 1877–1892 (2018).
25. S. Chen et al., High-efficiency lithium metal batteries with fire-retardant electrolytes. *Joule* **2**, 1548–1558 (2018).
26. X. Ren et al., Enabling high-voltage lithium-metal batteries under practical conditions. *Joule* **3**, 1662–1676 (2019).
27. X. Cao et al., Nonflammable electrolytes for lithium ion batteries enabled by ultra-conformal passivation interphases. *ACS Energy Lett.* **4**, 2529–2534 (2019).
28. H. Jia et al., High-performance silicon anodes enabled by nonflammable localized high-concentration electrolytes. *Adv. Energy Mater.* **9**, 1900784 (2019).
29. K. Dokko et al., Solvate ionic liquid electrolyte for Li-S batteries. *J. Electrochem. Soc.* **160**, A1304–A1310 (2013).
30. X. Zhang et al., Advanced electrolytes for fast-charging high-voltage lithium-ion batteries in wide-temperature range. *Adv. Energy Mater.* **10**, 2000368 (2020).
31. L. Cheng et al., Sparingly solvating electrolytes for high energy density lithium–sulfur batteries. *ACS Energy Lett.* **1**, 503–509 (2016).
32. K. Xu, Nonaqueous liquid electrolytes for lithium-based rechargeable batteries. *Chem. Rev.* **104**, 4303–4417 (2004).
33. B. D. Adams, J. Zheng, X. Ren, W. Xu, J.-G. Zhang, Accurate determination of coulombic efficiency for lithium metal anodes and lithium metal batteries. *Adv. Energy Mater.* **8**, 1702097 (2018).
34. X. Cao et al., Monolithic solid–electrolyte interphases formed in fluorinated orthoformate-based electrolytes minimize Li depletion and pulverization. *Nat. Energy* **4**, 796–805 (2019).
35. O. Borodin et al., Modeling insight into battery electrolyte electrochemical stability and interfacial structure. *Acc. Chem. Res.* **50**, 2886–2894 (2017).
36. N. Xiao, G. Gourdin, Y. Wu, Simultaneous stabilization of potassium metal and superoxide in K-O2 batteries on the basis of electrolyte reactivity. *Angew. Chem. Int. Ed. Engl.* **57**, 10864–10867 (2018).
37. H. Kim et al., In situ formation of protective coatings on sulfur cathodes in lithium batteries with LiFSI-based organic electrolytes. *Adv. Energy Mater.* **5**, 1401792 (2015).
38. T. A. Barnes, J. W. Kaminski, O. Borodin, T. F. Miller, Ab initio characterization of the electrochemical stability and solvation properties of condensed-phase ethylene carbonate and dimethyl carbonate mixtures. *J. Phys. Chem. C* **119**, 3865–3880 (2015).
39. E. R. Fadel et al., Role of solvent-anion charge transfer in oxidative degradation of battery electrolytes. *Nat. Commun.* **10**, 3360 (2019).
40. H. Sun, COMPASS: An ab initio force-field optimized for condensed-phase applications overview with details on alkane and benzene compounds. *J. Phys. Chem. B* **102**, 7338–7364 (1998).
41. G. Kresse, D. Joubert, From ultrasoft pseudopotentials to the projector augmented-wave method. *Phys. Rev. B* **59**, 1758–1775 (1999).

APPLIED PHYSICAL SCIENCES